

Nanoporous Crystal $12\text{CaO}\cdot 7\text{Al}_2\text{O}_3$: A Playground for Studies of Ultraviolet Optical Absorption of Negative Ions

Katsuro Hayashi,^{*,†} Peter V. Sushko,[‡] David Muñoz Ramo,[‡] Alexander L. Shluger,[‡] Satoshi Watauchi,[§] Isao Tanaka,[§] Satoru Matsuishi,[†] Masahiro Hirano,[†] and Hideo Hosono[†]

Materials & Structures Laboratory and Frontier Collaborative Research Center, Tokyo Institute of Technology, Yokohama 226-8503, Japan, Department of Physics & Astronomy, University College London, London WC1E 6BT, United Kingdom, and Center for Crystal Science and Technology, University of Yamanashi, Yamanashi 400-8511, Japan

Received: September 6, 2006; In Final Form: November 7, 2006

A novel nanoporous material $12\text{CaO}\cdot 7\text{Al}_2\text{O}_3$ (C12A7) offers a possibility of incorporating large concentrations ($>10^{21}\text{ cm}^{-3}$) of a wide range of extraframework anions inside its nanopores. We have investigated, both experimentally and theoretically, optical absorption associated with several types of such anions, including F^- , OH^- , O^- , O_2^- , O_2^{2-} , and assigned their optical absorption bands. It is demonstrated that the chemical identity and concentration of extraframework anions can be controlled by an appropriate treatment of “as grown” C12A7. We also show that the position of the adsorption edge is, in turn, determined by the chemical identity of the extraframework species and can be varied in the range of $\sim 4\text{--}6\text{ eV}$. We suggest that C12A7 is a unique host material, which can be used as a playground for studying negatively charged species that are unstable in other environments.

1. Introduction

A wide range of $\text{CaO}\text{--}\text{Al}_2\text{O}_3$ compounds have been studied for several decades. Their properties are considered to be well-established and they are routinely used in construction industries and other areas.¹ However, a novel material $12\text{CaO}\cdot 7\text{Al}_2\text{O}_3$ (C12A7)^{1–24} stands out of this family as its physical and chemical properties are very different from those of other $\text{CaO}\text{--}\text{Al}_2\text{O}_3$ -based compounds. For example, C12A7 can form a glass phase,² its lattice hosts a large concentration of unusual anion species, which are stable at a wide range of external conditions,^{3–15} and it is a fast ionic conductor.¹⁶ Finally, the fundamental absorption edge of C12A7 is much lower than that in other $\text{CaO}\text{--}\text{Al}_2\text{O}_3$ materials.¹⁷ These properties of C12A7 result from its unique crystalline structure: it consists of the *positively charged lattice framework*, which is compensated by *negative extraframework species*.¹⁸ The stoichiometric cubic unit cell with the lattice constant of approximately 1.2 nm (see Figure 1a) is represented by the formula $[\text{Ca}_{24}\text{Al}_{28}\text{O}_{64}]^{4+}\cdot 2\text{O}^{2-}$, where the first part denotes the framework built of 12 cages with inner free space of $\sim 0.4\text{ nm}$ each, while the O^{2-} ions are extraframework species that occupy 2 out of 12 framework cages.

As a result of this unusual structure there exists a large concentration of unoccupied cages ($\sim 5 \times 10^{21}\text{ cm}^{-3}$) each having positive charge of $+1/3\text{ |e|}$. As we discuss below, this has a dramatic effect on the electronic structure of this material. Moreover, a wide variety of negatively charged extraframework species can be incorporated into C12A7 at concentrations much higher than usual defect concentrations in solids. This allows one (i) to modify the properties of C12A7 by varying the content of the extraframework species and (ii) to use C12A7 host as a

playground for studying exotic anion species, which are either unstable or exist at low concentrations in other systems including “exotic” interstitial species.

It has been demonstrated that the extraframework O^{2-} ions can be partially or completely replaced by other oxygen-containing anions such as OH^- ,^{3,4} O_2^- ,^{8–10} O^- ,^{9,10} and O_2^{2-} ,^{11,12} as well as extrinsic species, e.g., F^- ,^{5,6} Cl^- ,^{5,7} H^- ,¹³ and Au^- .¹⁴ Furthermore, when C12A7 is subjected to severe reducing conditions, all extraframework ions can be replaced by electrons leading to the formation of a stable inorganic electride, where the extraframework electrons serve as anions.¹⁵ Monovalent anions occupy $1/3$ of the total number of cage sites, which corresponds to the anion concentration of $2.3 \times 10^{21}\text{ cm}^{-3}$. C12A7 fabricated in an oxidizing atmosphere can accommodate a large amount of (up to $>10^{21}\text{ cm}^{-3}$) active oxygen anions including O_2^- , O^- , and O_2^{2-} . These ions are encapsulated in the framework cages and remain stable even at a few hundred degrees Centigrade. This is in a sharp contrast with the behavior of the same ions on metal-oxide surfaces or in the gas phase, where they are very reactive and hardly persist in ambient air.²⁹ Extraframework OH^- ions are likely to be the most stable substitutive anions, since they promptly replace the extraframework O^{2-} ions when the sample is treated in a wet atmosphere. Similarly, when C12A7 is treated in an F-containing atmosphere, extraframework F^- ions are readily formed. The results of our earlier theoretical and experimental studies demonstrate that apart from the usual valence and conduction bands associated with the framework, C12A7 has a narrow band of unoccupied s-like states associated with the empty cages (see Figure 1b). Spatial distribution of the charge density due to several states of this band, as calculated using the periodic model approach described earlier,²¹ is shown in Figure 1c. An unusual feature of this band is that its states are not associated with any particular lattice atoms, like, for example, the 4f-band of Ce in CeO_2 . Instead, they can be characterized as states of a “particle in a

* Corresponding author. E-mail: k-hayashi@lucid.msl.titech.ac.jp.

[†] Tokyo Institute of Technology.

[‡] University College London.

[§] University of Yamanashi.

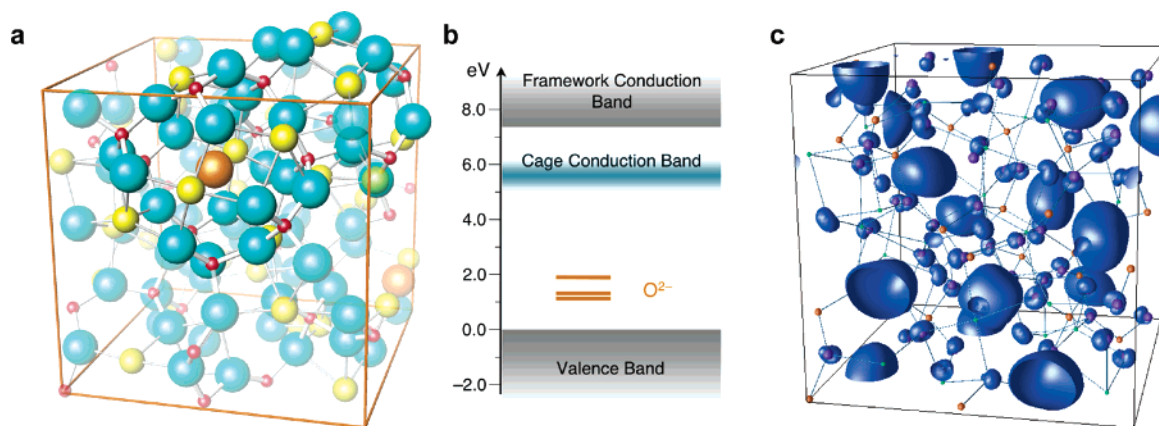


Figure 1. Crystal and electronic structure of C12A7. (a) Crystal structure of C12A7. Yellow, red, and light blue spheres indicate Ca, Al, and O, respectively. The orange frame indicates the cubic unit cell, which contains two C12A7 molecules and has the lattice constant of ~ 1.2 nm. The highlighted part is a pair of neighboring cages that are connected through an Ca–O–Al–O–Al–O opening. Note that parts of the two complete cages extend to outside of the unit cell. Each cage is coordinated by 8 first-neighboring cages. Extraframework O^{2-} ions that occupy 2 of 12 cages are indicated by orange spheres. (b) Electronic structure of stoichiometric C12A7 containing extraframework O^{2-} ions only. The relative positions of the bands and 2p states of the extraframework O^{2-} are determined by one-electron energies (see Section 4). (c) Charge density associated with several unoccupied states of the cage conduction band. The black frame indicates the cubic unit cell. The blue areas show the surfaces of the constant charge density. These areas are located in centers of unoccupied cages.

TABLE 1: Sample Annealing Conditions

no.	atmosphere	temperature profile
1	dry oxygen	1350 °C for 12 h, cooled with $50\text{ °C} \cdot \text{h}^{-1}$
2	wet air, $p(\text{H}_2\text{O}) = 0.04$ atm	1200 °C for 24 h, cooled with $50\text{ °C} \cdot \text{h}^{-1}$
3	wet He, $p(\text{H}_2\text{O}) = 0.02$ atm	1000 °C for 80 h, quenched
4	wet He, $p(\text{H}_2\text{O}) = 0.02$ atm	1200 °C for 15 h, quenched
5	wet He, $p(\text{H}_2\text{O}) = 0.02$ atm	1350 °C for 6 h, quenched
6	wet He, $p(\text{H}_2\text{O}) = 1 \times 10^{-3}$ atm	1350 °C for 6 h, quenched
7	CaF_2 vapor ^a	1100 °C for 240 h, quenched
8–12 ^b	wet He, $p(\text{H}_2\text{O}) = 0.02$ atm	1000 °C for 0.5–48 h, quenched

^a Annealed in a silica-glass ampule encapsulated with CaF_2 powder. ^b Sample 7 was used as a starting material. The annealing and the optical measurements were performed sequentially.

box”, where the “box” is formed by the cage wall. Thus, this band is referred to as *cage conduction band* or CCB. The CCB is located approximately 1–2 eV below the band of unoccupied states associated with the framework (*framework conduction band* or FCB).^{19–21} In the following we will use notations VB and FCB to refer to the states at the top of the valence band and at the bottom of the framework conduction band, respectively.

Ultraviolet (UV) irradiation of this material is expected to induce several types of electronic transitions: (i) from encaged anions to the FCB, (ii) from encaged anions to the CCB, (iii) from the VB to encaged anions, and (iv) intraanionic transitions. Our previous results have also shown that the extraframework ions deform the surrounding cage wall, thereby inducing a structural inhomogeneity in the lattice. Such an inhomogeneity is expected to affect noticeably optical transitions associated with the intrinsic energy bands as it does the ionic and electronic transport characteristics.

In this study, we have investigated the ultraviolet and visible (UV–vis) optical absorptions of C12A7 incorporating several kinds of anions. We focus on O^{2-} , OH^- , F^- , O_2^- , O^- , and O_2^{2-} ions in this work. None of these anions in C12A7 have been investigated by the optical absorption spectroscopy in the previous works. The presence and the concentrations of these ions can be determined by using several characterization techniques including IR spectroscopy, Raman scattering, and electron paramagnetic resonance (EPR). Moreover, relative concentrations of these species are well controlled by suitable thermal annealing treatments in oxygen, steam, and fluorine atmospheres. Anions formed under reducing conditions, specif-

ically H^- and electrons, are not treated in this study, because the detailed investigation of their optical properties has been published elsewhere.^{19,20} Our experimental results, together with theoretical calculations, demonstrate that the position of the absorption edge of C12A7 strongly depends on the chemical composition of the extraframework species. We describe the electronic structure of several extraframework species and establish the nature of the transitions responsible for the observed absorption bands. We also discuss a strong effect of the lattice inhomogeneity on the Urbach tail of the fundamental absorption edge in this material.

2. Evaluation of Extraframework Anion Concentrations

2.1. Sample Preparation and Evaluation Methods. Twelve C12A7 samples with different kinds and concentrations of the encaged anions were used in this work. Samples 1 and 2 were prepared from single crystals,^{22,23} while samples 3–12 have been obtained from transparent polycrystalline ingots of C12A7 grown or refined by a floating zone method. The samples were sliced into $\sim 3 \times 3$ mm pieces and then the slices were ground and polished to 50–200 μm thick plates with mirror surfaces. To control the incorporation of extraframework anions, these C12A7 plates were annealed in an alumina tube furnace under several conditions as listed in Table 1. Steam partial pressure, $p(\text{H}_2\text{O})$, in the atmosphere was regulated by bubbling air gas through water at ~ 30 °C (sample 2) or passing helium gas through a humidifier (samples 3–6 and 8–12). A dew point meter was used to monitor $p(\text{H}_2\text{O})$. Sample 7 was prepared by annealing a polycrystalline ingot at 1100 °C for 240 h in a silica-glass ampule encapsulated with CaF_2 powder (99.99% purity,

TABLE 2: Concentration of Extraframework Anions

no.	concentration (cm ⁻³)					
	OH ⁻	O ₂ ⁻	O ⁻	O ₂ ²⁻	O ²⁻	F ⁻
1	$(1.9 \pm 0.1) \times 10^{20}$	$(7 \pm 2) \times 10^{19}$	$(2 \pm 1) \times 10^{19}$	$(4 \pm 2) \times 10^{20}$	$(6 \pm 2) \times 10^{20}$	— ^a
2	$(2.3 \pm 0.1) \times 10^{21}$	$(1.8 \pm 0.5) \times 10^{18}$	< ^b	<	$(1 \pm 1) \times 10^{19}$	—
3	$(2.3 \pm 0.1) \times 10^{21}$	<	<	<	$(3 \pm 10) \times 10^{19}$	—
4	$(1.7 \pm 0.1) \times 10^{21}$	<	<	<	$(2.9 \pm 0.3) \times 10^{20}$	—
5	$(1.0 \pm 0.1) \times 10^{21}$	<	<	<	$(6.5 \pm 0.2) \times 10^{20}$	—
6	$(3.2 \pm 0.1) \times 10^{20}$	<	<	<	$(1.0 \pm 0.1) \times 10^{21}$	—
7	<	—	—	—	—	$(2.3 \pm 0.1) \times 10^{21}$
8	$(9.5 \pm 0.5) \times 10^{19}$	—	—	—	$(1 \pm 1) \times 10^{19}$ ^c	$(2.2 \pm 0.1) \times 10^{21}$
9	$(5.8 \pm 0.2) \times 10^{20}$	—	—	—	$(1 \pm 1) \times 10^{19}$ ^c	$(1.8 \pm 0.1) \times 10^{21}$
10	$(1.3 \pm 0.1) \times 10^{21}$	—	—	—	$(1 \pm 1) \times 10^{19}$ ^c	$(1.0 \pm 0.1) \times 10^{21}$
11	$(1.9 \pm 0.1) \times 10^{21}$	—	—	—	$(2 \pm 1) \times 10^{19}$ ^c	$(4.3 \pm 0.7) \times 10^{20}$
12	$(2.2 \pm 0.1) \times 10^{21}$	—	—	—	$(2 \pm 1) \times 10^{19}$ ^c	$(1.4 \pm 0.7) \times 10^{20}$

^a —: assumed to be less than 1×10^{18} cm⁻³ by taking into account the preparation conditions. ^b <: Evaluated to be less than 1×10^{18} cm⁻³ by EPR or Raman measurements. ^c Rough estimation from the absorption tail in Figure 6.

Kojyund Chemical Laboratory, Japan). This treatment provides an effective incorporation of extraframework F⁻ ions in C12A7 matrix. Relevant surface reaction layers were removed from the sample plates before optical absorption measurements.

2.2. Evaluation of OH⁻ Ion Concentration by IR Spectroscopy. IR spectra at 2000–3600 nm were measured with a Hitachi U4000 spectrophotometer in a transmission mode. Concentration of OH⁻ ions was evaluated from the intensity of the OH-stretching band at 3540 cm⁻¹ in the IR spectra and by using its molar integral extinction coefficient, $1.31(\pm 0.04) \times 10^3$ M⁻¹·cm⁻², reported earlier in ref 4. In the case of sample 2, which has been annealed in the most severely humidified atmosphere, the OH⁻ concentration has almost reached its maximum possible value as defined by the positive charge of lattice framework. Concentrations of OH⁻ ions in samples 3–6 were somewhat below the maximum possible value (see Table 2). No OH⁻ ions have been detected in sample 7.

2.3. Evaluation of O⁻ and O₂⁻ Concentrations by Electron Paramagnetic Resonance. EPR signals of crushed powder samples were measured at 77 K with a Bruker E580 spectrometer (X-band, ~9.7 GHz). Among the extraframework anions investigated in this study, only O₂⁻ and O⁻ oxygen radicals are EPR active because they have an unpaired electron spin of $S = 1/2$. The total spin concentrations in the samples were determined from the intensities of the second integral of the powder pattern spectra by using the CuSO₄·5H₂O crystal as a reference system. This evaluation introduces an error of ±10%. The concentration ratio between O₂⁻ and O⁻ was determined by a deconvolution of the EPR spectra as described in ref 9. This procedure gives rise to an additional error of ±20% in the evaluation of the absolute concentrations of O₂⁻ and O⁻.

Figure 2 shows EPR spectra obtained for samples 1 and 2. Sample 2 shows a typical powder pattern of O₂⁻, which has Lorentzian line shape and characteristic g -values of $g_{xx} = 2.002$ (± 0.001), $g_{yy} = 2.008$ (0.001), and $g_{zz} = 2.074$ (0.001).⁹ The total spin concentration of $\sim 2 \times 10^{18}$ cm⁻³ was obtained for sample 2, while in sample 1 it was larger by more than a factor of 40. EPR spectra measured for sample 1 were decomposed by using the calculated powder patterns for O⁻ with g -values of $g_{xx} = g_{yy} = 2.036$ (0.005) and $g_{zz} = 1.994$ (0.01).⁹ The ratio of O⁻ and O₂⁻ was evaluated from the intensities of the corresponding patterns giving the best fit to the measured spectrum as shown in the spectrum labeled 1' in Figure 2. In sample 2, the concentration of O₂⁻ was only 10⁻³ of that of OH⁻, i.e. formation of O₂⁻ ions was suppressed to the residual impurity level by the near-complete incorporation of OH⁻ ions.

On the contrary, a dry oxygen atmosphere promotes formation of oxygen radicals. However, even in this case their total

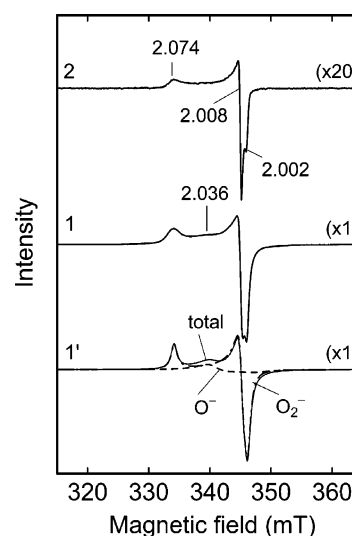


Figure 2. EPR spectra of samples annealed in dry oxygen (No. 1) and in wet air (No. 2). The solid curve in spectrum 1' is a simulation of the experimental spectra for sample 1, which is reproduced by a superposition of the powder patterns for O₂⁻ (point-dashed line) and O⁻ (dashed line).

concentrations in single crystals are about ten times smaller than those in low-density polycrystals subjected to similar annealing conditions.⁹ This difference is explained by the formation process of the oxygen radicals: they are formed by uptake of oxygen gas from the surface and subsequent inward chemical diffusion.¹⁰ Thus, a dense crystal requires longer annealing time to accommodate the same amount of oxygen radicals, as compared with a fine-grained ceramics, due to a smaller effective surface area and a larger bulk size. Oxygen radical concentration was less than 1×10^{18} cm⁻³ in other samples (Nos. 3–12), which were annealed in helium atmosphere, indicating that the elimination of oxygen in atmosphere efficiently suppresses the formation of oxygen radicals.

2.4. Raman Spectroscopy and Evaluation of O₂²⁻ Concentration. Raman spectra were measured in powdered samples at room temperature using a Nicolet 960 Fourier transformation spectrometer with a YAG laser ($\lambda = 1.064$ μm) as an excitation light source. Figure 3 shows Raman spectra of samples 1, 2, and 4. The spectrum of sample 4 is shown as a representative one for samples 3–12. The presence of O₂⁻ in sample 1 is confirmed by a Raman band at 1128 cm⁻¹, which is attributed to the stretching vibration of O₂⁻.²⁹ The concentration of O₂⁻ ions in samples 2 and 4, as evaluated by EPR, was only ~1/30 and <1/70 of that in sample 1, respectively. Consequently, the

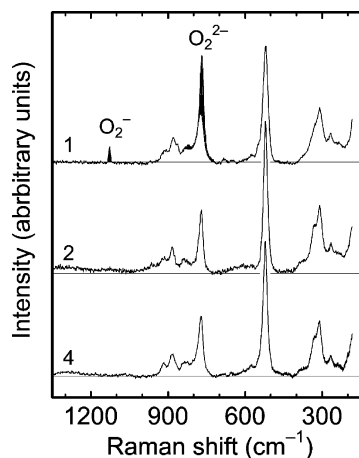


Figure 3. Raman spectra of samples annealed in dry oxygen (No. 1), wet air (No. 2), and wet He (No. 4), normalized to the intensity of the 520 cm^{-1} band. Peaks corresponding to O_2^- and O_2^{2-} are indicated by shaded area.

O_2^- signal is not detected clearly by Raman spectroscopy in these samples.

Raman spectrum profiles in a range $200\text{--}1000\text{ cm}^{-1}$, and are attributed to the vibrations of the lattice framework,³⁰ are nearly the same among the three samples. However, the intensity of the $\sim 770\text{ cm}^{-1}$ band of sample 1 differs markedly from those of other samples, suggesting a band due to an oxygen-derived anion is superposed on a lattice band at this frequency. Moreover, the peak position of the superimposed band, indicated with the shaded area in Figure 3, and that of the base band are separated by $\sim 2\text{ cm}^{-1}$, indicating that they have different origin. The superposed band, with a peak at 768 cm^{-1} , has been attributed to the peroxide ion (O_2^{2-}),^{11,12,29} while the base band at 770 cm^{-1} is due to the lattice framework. Although O_2^{2-} ions are not detectable by EPR, their concentration (see Table 2) can be estimated from the relationship between the intensity of the superposed band and weight loss, caused by a decomposition of the O_2^{2-} ion, determined by a thermogravimetric analysis.¹²

2.5. Evaluation of Fluoride Ion Concentration. No evaluation techniques employed in this study can detect F^- ions directly. However, their concentrations were estimated by subtracting the combined charge of other extraframework anions (OH^- , O^{2-} , O_2^- , O^- , and O_2^{2-} ions) from the total charge required to compensate the positive charge of the lattice framework ($2.3 \times 10^{21}\text{ cm}^{-3}$).

Neither OH^- ions nor oxygen radicals were detected in sample 7, which was subjected to prolonged CaF_2 treatment. We tentatively assumed that sample 7 contains less than 10^{19} cm^{-3} extraframework O^{2-} ions. Thus, the concentration of F^- ions in sample 7 is determined to be $2.3 \times 10^{21}\text{ cm}^{-3}$. The presence of only small amount of O^{2-} incorporated into sample 7 will be confirmed by the fact that sample 7 exhibits much higher absorption edge energy than O^{2-} incorporating samples. It was further observed that the F^- ions could be replaced by OH^- due to the wet He annealing (samples 8–12).

The concentrations of extraframework anions determined for each sample are listed in Table 2. It is firmly established that active oxygen anions such as O_2^- , O^- , and O_2^{2-} were only generated upon annealing C12A7 in O_2 -containing atmosphere. Annealing C12A7 in the wet He atmosphere resulted in the formation of both OH^- and O^{2-} extraframework ions, while annealing in high humidity He gas for long times produces almost exclusively OH^- ions (sample 12). On the other hand,

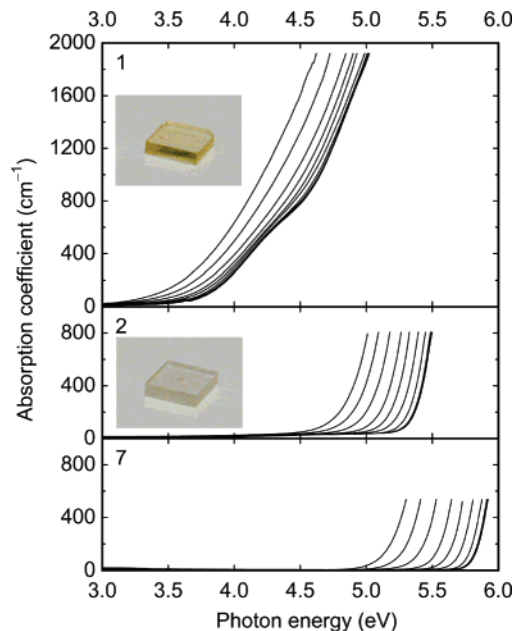


Figure 4. Absorption spectra of samples annealed in dry oxygen (No. 1), in wet air (No. 2), and annealed in a silica-glass ampule encapsulated with CaF_2 (No. 7). Measurement temperatures were 8, 20, 40, 77, 150, 225, 298, 373, 473, 573, and 673 K . All samples show the shift of the absorption edge to lower energy with increasing temperature. Insets are photographs of samples equivalent to 1 and 2 under heating to $\sim 200\text{ }^\circ\text{C}$, demonstrating the yellow coloration due to the incorporation of active oxygen anions.

the prolonged CaF_2 treatment allowed us to replace all the extraframework anions by F^- ions (sample 7) and subsequent -He annealing further replaced the F^- ions by OH^- ions (samples 8–12, see Supporting Information).

3. Optical Absorption

3.1. Method. UV–vis optical absorption spectra at $200\text{--}800\text{ nm}$ were measured with a Hitachi U4000 spectrophotometer in a transmission mode. The dependence of the UV absorption on the relative orientations of the crystal axis and the light polarization has not been considered in this study. A cryostat was used to measure the temperature dependence of UV–vis spectra at $8\text{--}225\text{ K}$. The measurements at $298\text{--}673\text{ K}$ were carried out in air with use of an electrical furnace designed for the optical spectroscopy. Spectra obtained at room temperature before and after the heating to 673 K were found to be identical. We therefore concluded that the heating and consecutive cooling of C12A7 samples induces no significant changes in the concentrations of the extraframework anions.

3.2. Extraframework Anions and Temperature Dependence of UV Absorption Edge. Temperature dependences of UV–vis spectra for samples 1, 2, and 7 are shown in Figure 4. The absorption edge shifts to lower energies with increasing temperature in all samples. Sample 1, which contains active oxygen anions, shows the lowest absorption edge energy among the three. Upon heating above $\sim 200\text{ }^\circ\text{C}$, sample 1 became tinted with yellow, corresponding to an increase in the absorbance at around 3 eV caused by the temperature-induced shift of the absorption edge to the visible energy range (see insets of Figure 4). Such coloration has not been observed in C12A7 with small concentrations of the active oxygen anions nor in other calcium aluminate compounds to our knowledge. We note that the position of the absorption edge depends strongly on the type of dominant extraframework species. The edge shifts to higher energies in the case of sample 2, which contains almost

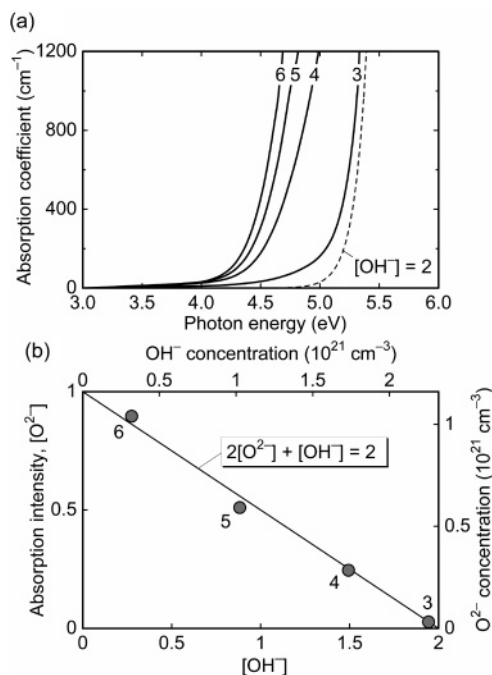


Figure 5. UV photoabsorption of the extraframework O^{2-} ions. (a) Absorption spectra for samples annealed in wet He atmosphere (Nos. 3–6) measured at 298 K. Dashed line corresponds to $[\text{OH}^-] = 2$. (b) Relationship between $[\text{OH}^-]$ evaluated from IR absorption and intensity of UV absorption bands shown in part a. Linear dependence corresponds to the relationship $2[\text{O}^{2-}] + [\text{OH}^-] = 2$, supporting the assignment of the observed absorptions to extraframework O^{2-} ions.

exclusively extraframework OH^- ions, and even further to higher energies in the case of sample 7, which contains predominantly F^- ions. Thus, the position of the absorption edge is defined by the extraframework species.

3.3. Optical Absorption of Oxide and Hydroxide Ions.

Figure 5a shows UV absorption spectra of samples 3–6, which contain only OH^- and O^{2-} extraframework ions. The condition of the electroneutrality implies that the following relationship between the concentrations of the two species holds

$$2[\text{O}^{2-}] + [\text{OH}^-] = 2 \quad (1)$$

where brackets denote the content of extraframework anions per one mole of C12A7 framework. It is found that the absorption edge shifts to lower energy side with a decrease in OH^- and simultaneous increase in O^{2-} ion content. The dashed line shows the estimated absorption of C12A7 containing exclusively extraframework OH^- ions ($[\text{OH}^-] = 2$), which was obtained by fitting a shifted exponential function to the spectrum of sample 2 in the spectral region with the absorption coefficient $\alpha > \sim 100 \text{ cm}^{-1}$. Therefore, deviations of the absorption spectra from the dashed line are considered to be associated with the extraframework O^{2-} ions.

Since the whole spectral region of the extraframework O^{2-} ions cannot be accessed properly due to the strong absorption intensity in the high-energy region, we applied the following procedure. First, the observed tails of absorption bands were fitted by using the shifted exponential function. The integrated intensity at the measured photon energy range ($\sim 3\text{--}5.3 \text{ eV}$) has been used as a measure of the total absorption intensity due to extraframework O^{2-} ions. Figure 5b shows the relative integrated intensities plotted against the OH^- content. A clear linear relationship between the two values confirms that the deviated part of the observed optical absorption is associated with the extraframework O^{2-} ions.

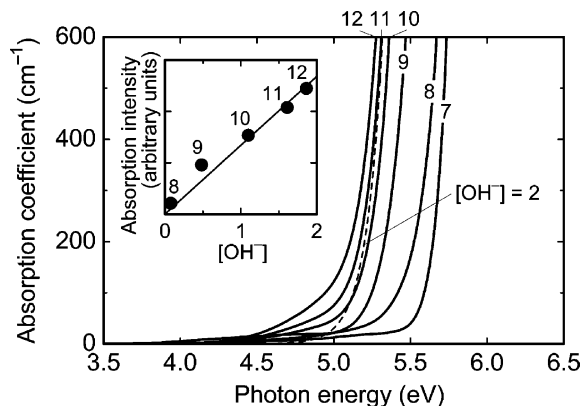


Figure 6. Absorption spectra of the F-substituted sample (No. 7) and those reannealed in wet He atmosphere (Nos. 8–12) measured at 298 K, showing absorption of the extraframework OH^- ion. The dashed line corresponds to $[\text{OH}^-] = 2$. The inset shows the relationship between $[\text{OH}^-]$ evaluated from IR absorption and the intensity of the UV absorption band. A linear dependence validates the assignment of the absorption tail to the extraframework OH^- ions.

Figure 6 shows UV absorption spectra of sample 7 (fluorine-substituted C12A7) and samples 8–12, which were prepared by reannealing of sample 7 in wet He atmosphere. The IR spectroscopy measurements verify that the concentration of OH^- ions in sample 7 is below the detection limit of $1 \times 10^{18} \text{ cm}^{-3}$. The results of our theoretical calculations (see Section 4) indicate that the energy level of the engaged F^- ion is located below the top of the VB. Thus, the observed absorption edge in sample 7 is associated with the electronic excitations from VB to FCB, while the F^- ions are not directly involved in these transitions.

Taking the absorption spectrum of sample 7 as a reference, the extra intensities associated with the absorption spectra of samples 8–12, where the OH^- ion content increases gradually from sample 8 to sample 12 (see Table 2), were evaluated by exponential fitting in a similar manner to that used for the case of O^{2-} . The inset in Figure 6 shows the relationship between the $[\text{OH}^-]$ evaluated from the IR spectroscopy and the absorption intensity obtained by the exponential fitting. The good linear relationship between them indicates the red shift of the optical absorption spectra in samples 8–12 is due to the increase in the concentration of extraframework OH^- ions.

The absorption spectrum of C12A7 with $[\text{OH}^-] = 2$ is plotted as a dashed line in Figure 6. It is noted that absorption spectra of samples 11 and 12 are shifted to lower energies with respect to the dashed line even though the corresponding values of $[\text{OH}^-]$ are less than 2. This shift is attributed to the presence of extraframework O^{2-} ions. Indeed, the absorption spectra of samples 11 and 12 are very similar to that of sample 3, which contains a small amount of the O^{2-} ions ($3 \times 10^{19} \text{ cm}^{-3}$). It is also expected that a small amount of oxygen was incorporated in C12A7 during thermal annealing of these samples. As listed in Table 2, the content of O^{2-} ions in samples 8–12 is estimated to be 1×10^{19} to $2 \times 10^{19} \text{ cm}^{-3}$ from the surplus absorption. In addition, Mie scattering may slightly affect the absorption spectra of these samples.²⁵

3.4. Optical Absorption of Active Oxygen Anions. Figure 7 shows the absorption spectrum of sample 1 at 8 K, together with calculated partial contributions of OH^- and O^{2-} ions and Urbach tail (see section 5.2). The fundamental absorption due to the transition from the VB to FCB (intrinsic absorption) is also shown. The difference between the spectrum measured for sample 1 and that for C12A7 containing only extraframework O^{2-} ions is shown with a point-dashed line. This difference forms a broad band, which is attributed to the absorption of

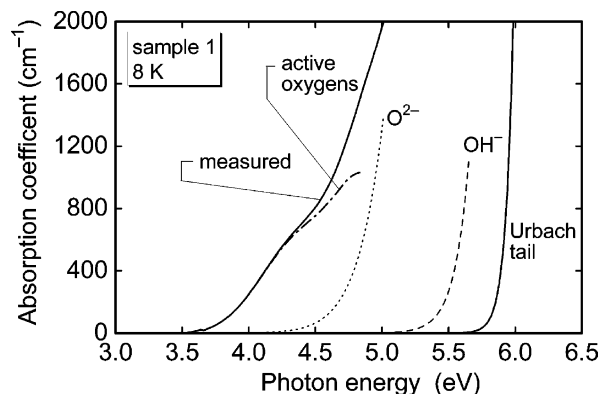


Figure 7. Contributions due to Urbach tail, extraframework OH^- and O^{2-} ions, and active oxygen anions (O_2^{2-} , O_2^- , and O^-) to the absorption spectra of sample 1 at 8 K. Bold solid, thin solid, point, and dashed lines indicate measured spectrum, Urbach tail obtained from spectrum of sample 7, the O^{2-} band, and the OH^- band calculated from O^{2-} and OH^- content ($[\text{O}^{2-}] = 0.52$, $[\text{OH}^-] = 0.16$), respectively. The dashed-point line was obtained by subtraction of the O^{2-} absorption from the measured one and corresponds to the absorption due to active oxygen anions.

active oxygen anions O_2^- , O^- , and O_2^{2-} together. The active oxygen anions band seems to consist of two components: bands 1 and 2. Band 1 appears as a shoulder with a peak position at ~ 4.2 eV. The peak of band 2 was not directly observable due to the strong absorption intensity in the higher energy side. Assuming the Gaussian-type band profile, the peak position is estimated to be higher than 4.7 eV.

4. Theoretical Assignment of the Optical Absorption of the Extraframework Anions

4.1. Method. Atomistic structure and electronic properties of several extraframework anion species in C12A7 have been investigated by using ab initio calculations and an embedded cluster approach. The details of the methodology as applied to C12A7 have been described earlier.¹⁹ In brief, C12A7 is represented atomistically by using a finite system of ~ 7500 atoms referred to as nanocluster (NC). The NC is divided into two regions: polarizable spherical region I at the center of the NC and the remaining part of the NC, nonpolarizable region II. By construction region I is centered on a “site of interest”, which, together with neighboring lattice atoms, is considered quantum mechanically (QM cluster). The QM cluster is interfaced with the remaining part of region I, which is represented by using classical interatomic potentials.²⁶ The total energy includes contributions due to (i) the energy of the QM cluster in the electrostatic potential of the rest of the system, (ii) the interatomic interaction, both Coulomb and short-range, of classical atoms in regions I and II, (iii) the non-Coulomb part of the interaction between the classical atoms and atoms of the QM cluster, and (iv) the semilocal embedding potential associated with the interface atoms.

To determine the equilibrium structures of the extraframework species we used QM clusters comprising one or two cages where one of the cages was occupied by an extraframework ion. The total energy of the system was minimized with respect to the coordinates of all atoms in region I (~ 700 atoms), both quantum and classical, while atoms in region II remained fixed at their corresponding bulk positions. This approach allows us to account explicitly for the defect-induced lattice deformation as well as to incorporate the effect of this deformation on the defect itself. The method is implemented in the Guess computer code²⁷ and

uses the Gaussian package²⁸ for calculations of the quantum-mechanical contributions to the total energy and forces.

The QM calculations were carried out with use of a hybrid density functional B3LYP and 6-31G and LANL2DZ basis sets for anions (O and F) and cations (Ca and Al), respectively. Time-dependent density functional theory (TDDFT), as implemented in the Gaussian package,²⁸ was used to calculate optical absorption energies and the corresponding transition dipole matrix elements.

4.2. Local Atomic Structure of Extraframework Species.

The detailed description of the local geometry of all extraframework species considered in this work (O^{2-} , OH^- , O_2^{2-} , O^- , O_2^- , and F^- ions) is beyond the scope of this paper. However, it is instructive to consider generic features of these structures such as position and, in the case of molecular ions, orientation of the extraframework species and their effect on the lattice relaxation. It is convenient to characterize the effect of the extraframework species on the C12A7 lattice by using the distance between the axial Ca ions of the corresponding cage, d_{S4} , where subscript S4 defines the cage symmetry axis S_4 . In the case of the empty cage d_{S4} is close to 5.54 Å and it decreases on average to 4.89 Å in the cages occupied by monovalent anions (OH^- , O^- , O_2^- , and F^-). The deformation of the cage wall is even stronger if the cage contains divalent anions (O^{2-} or O_2^{2-}) in which case d_{S4} decreases on average to 4.48 Å. Monoatomic anions O^- and F^- , as well as molecular ions O_2^{2-} and O_2^- , occupy on-center sites close to the middle of the S_4 axis. Molecular ions O_2^{2-} and O_2^- are oriented roughly perpendicular to the S_4 axis. In the case of OH^- , the oxygen atom is approximately at the cage center, while the proton is oriented toward one of the oxygen ions in the cage wall and forms a hydrogen bond with it. Overall, the OH^- axis is also approximately perpendicular to the S_4 axis of the cage. Finally, the O^{2-} ion induces the strongest deformation of the cage wall as compared to other extraframework ions. It occupies an off-center configuration in which it is displaced toward the cage wall and forms a bond with one of the Al ions. As a result, this Al as well as two axial Ca atoms displace toward the cage center.²¹ In all subsequent calculations we used the geometries of fully relaxed systems.

4.3. Vibration Frequencies of Extraframework Oxygen Anions. We calculated the frequencies of the stretching mode vibrations for the extraframework O_2^- and O_2^{2-} ions using numerical differentiation of the potential energy surface with respect of coordinates of the two corresponding atoms. The stretching frequencies calculated for O_2^- and O_2^{2-} are 1039 and 784 cm^{-1} , respectively. These values are in a respectable, although not perfect, match with experimentally observed Raman shifts at 1128 and 768 cm^{-1} . Nevertheless, the agreement is solid enough to support the assignment of these Raman shifts to extraframework O_2^- and O_2^{2-} , respectively.

4.4. Absorption Energies and the Nature of the Transitions. The TDDFT calculations for QM clusters containing unoccupied cages only suggest that two types of band-to-band UV electronic excitations can be associated with the C12A7 framework: transitions from the valence band to (i) an s-like state of the cage conduction band ($\text{VB} \rightarrow \text{CCB}$) and (ii) to the states of the framework conduction band ($\text{VB} \rightarrow \text{FCB}$). Fifteen lowest energy $\text{VB} \rightarrow \text{CCB}$ transitions have been investigated. We found the lowest, and very weak, transition at 5.2 eV, while a few much stronger transitions appear at higher energies of 5.7, 6.0, and 6.2 eV, where the edge of the corresponding absorption band begins to develop. The lowest energy $\text{VB} \rightarrow \text{FCB}$ transition is found at 6.8 eV.

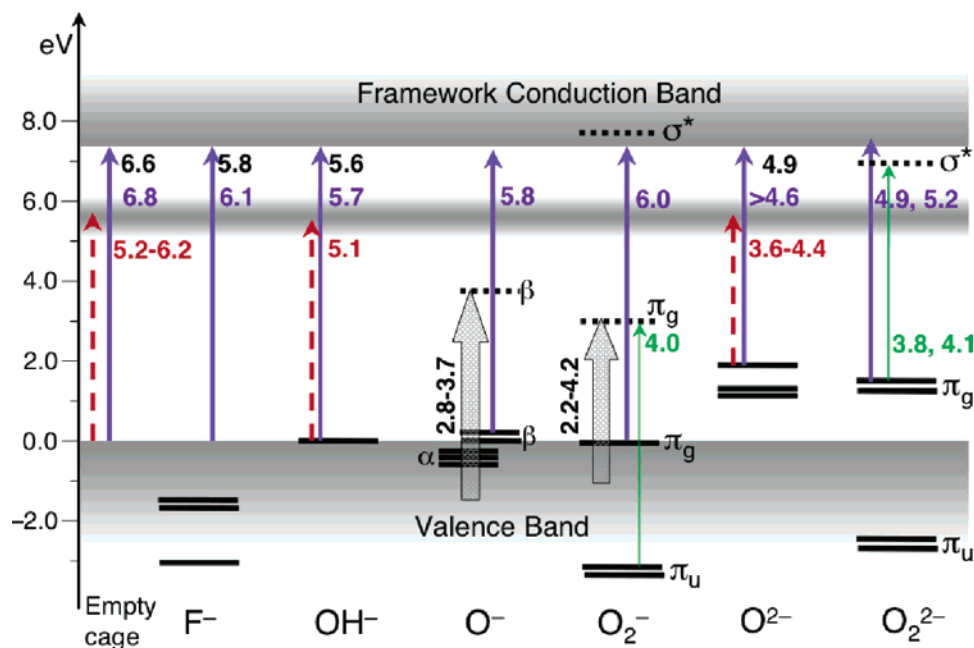


Figure 8. One-electron energy levels and excitation energies determined for C12A7 containing different extraframework anions. The cage conduction band is shown as a horizontal gray bar just below 6 eV. The diagram has two energy scales: (i) the positions of the band edges and one-electron energy levels are shown with the scale on the left and (ii) the excitation energies of optical transitions calculated by using TD-DFT are shown with vertical arrows and corresponding numbers (in eV). Bold solid arrows and the numbers in the top two rows show the transition to the FCB states determined experimentally (top row, black) and theoretically (second row, blue), respectively. Transitions to the CCB states (third row, red) are shown with dashed lines. Intramolecular transitions for O_2^- and O_2^{2-} ions are shown with thin solid lines (fourth row, green). Finally, the transitions from the VB states to the unoccupied states of the oxygen radicals are shown with wide gray arrows. Black solid and dashed bars indicate occupied and unoccupied levels, respectively.

In general, the excitation energies of $\text{VB} \rightarrow \text{CCB}$ and $\text{VB} \rightarrow \text{FCB}$ transitions depend on the extraframework species occupying C12A7 cages. However, in all cases considered, with the exception of O^{2-} (see below), no CCB states were found for the cages occupied by the extraframework species. As a result, the $\text{VB} \rightarrow \text{CCB}$ transitions are associated with empty cages and their excitation energies are only weakly affected by the extraframework species. On the contrary, the onset of the $\text{VB} \rightarrow \text{FCB}$ transitions associated with occupied cages shifts to lower values depending on the type and charge state of the extraframework species. In our calculations the lowest excitation energy of the $\text{VB} \rightarrow \text{FCB}$ transitions was found to be in the range of 6.1–6.6 eV. For brevity, the band-to-band transitions will not be discussed separately for each extraframework anion.

In the following we describe the absorption energies associated with each type of extraframework species (see also the schematics of the transitions in Figure 8). The possible types of transitions already have been summarized in Section 1.

The extraframework F^- ion is the only anion species that does not contribute directly to the optical absorption spectrum and, therefore, it is convenient to describe its electronic structure first. The one-electron states associated with 2p states of F^- are mixed with the O 2p states of the valence band in the range of 1.5–3 eV below the top of the VB. The presence of F^- strongly distorts the CCB state associated with the cage and therefore $\text{VB} \rightarrow \text{CCB}$ transitions could not be clearly identified. The lowest calculated excitation energy of a $\text{VB} \rightarrow \text{FCB}$ transition is 6.1 eV. This energy is smaller than that found for the empty cage because the negative F^- ions perturb the 2p states of the cage wall oxygens and effectively shift the top of the VB to higher energy.

The case of an extraframework OH^- ion has been considered by using a 2-cage QM cluster, where one cage was occupied by OH^- and the other was empty. This allowed us to explicitly

account for the presence of a CCB state. We found that the lowest excitation energy of 5.1 eV corresponds to a charge-transfer transition in which an electron is transferred from the OH^- ion to a CCB state in a neighboring cage ($\text{OH}^- \rightarrow \text{CCB}$ type). The nature of this transition is identical to those discussed earlier for extraframework H^- ²⁰ and Au^- ¹⁴ ions. The intensity of this transition is, however, quite low due to a large spatial separation of the states associated with extraframework species and empty cages. We therefore do not consider transitions of this type for other extraframework species.

A stronger transition of the $\text{OH}^- \rightarrow \text{FCB}$ type is found at 5.7 eV. We note that this excitation energy is at the lower part of the absorption of the empty cages (see above) and therefore is expected to contribute to the absorption edge shift.

Since the extraframework O^{2-} also has an off-center configuration, there is a state localized in the same cage, which can be identified as a perturbed CCB state. Consequently, there are three $\text{O}^{2-} \rightarrow \text{CCB}$ transitions with calculated excitation energies of 3.7, 4.2, and 4.4 eV. The energy range of 4.6–5.6 eV is occupied by $\text{O}^{2-} \rightarrow \text{FCB}$ transitions only. At energies higher than 5.6 eV they begin to overlap with $\text{VB} \rightarrow \text{CCB}$ transitions and become difficult to detect.

The highest occupied one-electron states associated with extraframework O_2^- and O^- ions are at the very top of the VB. Consequently, the lowest excitation energies of transitions from the states of these ions to the FCB states are very close to each other: 6.0 eV for O_2^- and 5.8 eV for O^- . Two occupied π_g states of the doubly negatively charged O_2^{2-} are split from the top of the valence band and, as a result, the excitation energies of the $\pi_g \rightarrow \text{FCB}$ transitions begin at lower energies of 4.9 and 5.2 eV.

Another type of optical absorption, qualitatively different from those described above, was also found for active oxygen anions O_2^{2-} , O_2^- , and O^- . It is due to the transitions from the O 2p

states of the framework O ions to unoccupied states of the extraframework species. The unoccupied σ^* state of the O_2^{2-} ion is close to the bottom of the FCB and, therefore, these transitions begin at relatively high energy of about 6.0 eV. However, in the case of the singly charged ion O_2^- the unoccupied state π_g is very close to the top of the VB and the $VB \rightarrow \pi_g$ transitions begin at much lower energies. For example, 30 lowest excited states of this type calculated for O_2^- form the low-energy part of the optical absorption spectrum ranging from 2.2 to 4.2 eV. Similarly, in the case of the O^- ion, the excitation energies of 25 lowest excited states are in the region 2.8–3.7 eV, i.e., cover the same low-energy part of the optical absorption spectrum.

Finally, we describe intra-anion transitions found for the active anions. For the O^- ion we found two very weak $p \rightarrow p$ transitions at 0.3 and 0.8 eV. In the case of O_2^- only one strongly allowed transition ($\pi_u \rightarrow \pi_g$) was found at 4.0 eV. Intramolecular transitions $\pi_g \rightarrow \sigma^*$ (at 4.8 eV) and $\sigma \rightarrow \pi_g$ (at 6.2 eV) are prohibited even though they are coupled to the states of the framework. In the case of O_2^{2-} two weak $\pi_g \rightarrow \sigma^*$ transitions were found at 3.8 and 4.1 eV.

5. Discussion

We tentatively define the energy of the absorption edge, E_E , as energy where the absorption coefficient measured is equal to $\sim 1000 \text{ cm}^{-1}$. E_E of sample 7 (containing predominantly extraframework F^- ions) is the largest among all the samples examined in this study with a value of 5.9 eV. It is still lower than E_E observed in other calcium-aluminates ($> 6 \text{ eV}$). Furthermore, E_E in C12A7 strongly depends on the content of the extraframework species. That is, it is reduced to 5.6 eV by incorporation of OH^- ions, to 4.9 eV in the presence of O^{2-} ions, and further to 4.7 eV upon formation of the extraframework active oxygen anions. These E_E values are also indicated in Figure 8. In this section we discuss such dramatic shifts of the absorption edge, which is a peculiar feature of this material.

5.1. Extraframework Anions. (a) *Oxide Ion and Oxygen Radical Anions.* The C12A7 optical band gap, calculated theoretically as the excitation energy from the VB to the FCB states, is on the order of 6.1–6.8 eV depending on the encaged anion species. The extraframework O^{2-} ions shift the absorption edge down to 4.9 eV for $[O^{2-}] = 1$. This absorption is attributed to the $O^{2-} \rightarrow \text{FCB}$ transitions, which are the only type of transitions in the range of 4.6–5.6 eV according to theoretical calculations. The transitions of the $O^{2-} \rightarrow \text{CCB}$ type should be found at lower energies of 3.7–4.4 eV. These, however, are unlikely to contribute strongly to the absorption edge because of the low density of these transitions.

With the formation of the oxygen radicals (O^- , O_2^- , and O_2^{2-}) additional absorption bands appear at ~ 4.7 and 4.3 eV and the absorption edge shifts to lower energy due to their superposition as shown in Figure 7. Since the three extraframework species are present simultaneously, the definitive assignment of the absorption bands on the basis of the experimental data alone is problematic. We can, however, rule out the assignment of these bands to the transitions from the oxygen radicals to FCB states because their occupied levels are always deeper than those of the O^{2-} and therefore the corresponding excitation energies should have higher values.

Our theoretical calculations indicate that the possible candidates for these bands are the transitions from the VB to oxygen radicals and/or the intramolecule $\pi_u \rightarrow \pi_g$ transition of O_2^- . The assignment to the intermolecular transitions is consistent with reported observations that O_2^- ions exhibit UV absorption

bands ascribed to intramolecule transitions of $\pi_u \rightarrow \pi_g$ when incorporated in alkali halides (5.0 eV)^{35,36,39} and inert gas crystals (4.5–5.0 eV).⁴¹ The intramolecular $\pi_g \rightarrow \sigma^*$ transitions of O_2^{2-} ions also contribute to these bands, because the absorption of the O_2^{2-} ion occurs at 5.0 eV in BaO_2 , and that of the O_2^{2-} -anion vacancy complex is observed at 4.8 eV in alkali halides^{37,38} although their intensities are very small. Thus, it is tentatively concluded that the additional absorption bands at ~ 4.7 and 4.3 eV in the oxygen radical incorporated C12A7 are attributed to the transitions from the VB to oxygen radicals and/or the intramolecule transitions of O_2^- and O_2^{2-} .

(b) *Hydroxide Ion.* The OH^- ions provide the absorption edge at 5.6 eV for $[OH^-] = 2$ at room temperature. The intramolecular transition from the oxygen 2p orbital to the O–H antibonding state, whose energy is rather insensitive to host materials, occurs at $\sim 8 \text{ eV}$ in alkali halide and silica glass.⁴⁰ Further, the transition from the VB to OH^- should need much higher energy. Thus, the observed absorption can only be attributed to the transition from OH^- to the FCB, which agrees with the results of the calculations (5.7 eV). We note that the $OH^- \rightarrow \text{CCB}$ transitions with the calculated excitation energy of 5.1 eV can also contribute to the absorption edge shift to lower energies. The assignment of the 5.6 eV band to the transition from OH^- to the FCB is consistent with earlier studies of alkali halides.^{35–39} OH^- ions substituting anion sites exhibit absorption bands peaking at 5.6–6.6 eV, which have been assigned to the excitation from the oxygen 2p levels to the conduction bands. In accord with this assignment, the peak position shifts to lower energies for narrower band gap hosts.^{35,36,38}

5.2. Urbach Tail. Since the 2p states of the extraframework F^- ion are below the top of the VB, as revealed by the theoretical calculation, it does not contribute directly to the optical absorption spectrum and the observed absorption edge in the fluorine-doped C12A7 (sample 7) is attributed to the transition from the VB to the FCB or the fundamental absorption edge of the C12A7 framework. Figure 9a shows the dependence of the absorption coefficient (α) on the photon energy (E) in the fundamental absorption region of sample 7 for several temperatures. It is clearly shown that α varies exponentially with the photon energy. The slope of the $\ln \alpha$ decreases with temperature and extrapolations of these plots to higher photon energies made for different temperatures sharply converge at a focal point ($E_0 = 6.6 \text{ eV}$) with an absorption coefficient (α_0) of $6.1 \times 10^7 \text{ cm}^{-1}$. These facts clearly indicate the absorption is indeed due to the Urbach tail, where E dependence of α is given empirically by^{31–34}

$$\alpha = \alpha_0 \exp\left(\frac{E - E_0}{\Delta E}\right) \quad (2)$$

where ΔE represents the width of the exponential absorption tail depending on temperature known as the Urbach energy. Since the Urbach tail is caused by the exciton phonon interaction, the good convergence of the extrapolated lines indicates that the focal point energy E_0 corresponds to intrinsic exciton energy. Since the value of $E_0 = 6.6 \text{ eV}$ agrees with the calculated fundamental band gap of 6.1–6.8 eV, the exciton is associated with the FCB and VB. In other words, the observed absorption edge in sample 7 is attributable to the $VB \rightarrow \text{FCB}$ transitions, but not to those involving the F^- ion.

Here, the Urbach tail is analyzed in more detail by using Toyozawa's theory³¹ modified by Cody et al.³² Temperature dependence of the steepness parameter, $\sigma = kT/\Delta E$, is introduced to represent the fluctuation of a lattice due to the electron

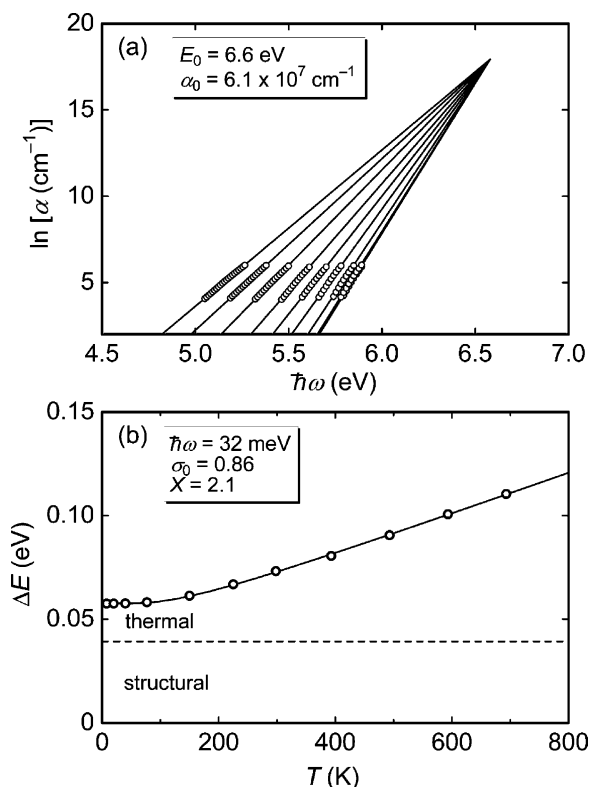


Figure 9. Analysis of Urbach tail measured for sample 7. (a) Semilogarithmic plot of the absorption coefficient against photon energy. (b) Temperature dependence of Urbach energy, ΔE . The solid line is obtained by fitting the parameter of the disorder model described by eq 3 to the data points shown with open circles. The dashed line separates contributions to the Urbach energy due to thermal fluctuations and structural disorder.

phonon interaction as given by

$$\sigma = \frac{2\sigma_0 kT}{\hbar\omega_0} \tanh\left(\frac{\hbar\omega_0}{2kT}\right) \quad (3)$$

where σ_0 is a constant value independent of temperature and $\hbar\omega_0$ is the characteristic phonon energy associated with the Urbach tail. Since the fluctuation is caused by thermal motion and structural disorder, eq 3 has been modified to

$$\Delta E = \frac{\hbar\omega_0}{2\sigma_0} \left[\coth\left(\frac{\hbar\omega_0}{2kT}\right) + X \right] \quad (4)$$

where X is a dimensionless measure of the structural disorder normalized to the zero-point vibration energy, $\hbar\omega_0/2$. Figure 9b shows ΔE as a function of temperature obtained by the best fitting of the spectra in Figure 9a to eq 4. As indicated by a fitted line in Figure 9b, the temperature change of ΔE is best described with $\sigma_0 = 0.86$, $\hbar\omega_0 = 32$ meV, and $X = 2.1$. A dashed line in Figure 9b separates contributions of the thermal fluctuation and the structural disorder to ΔE . It is found that the Urbach tail in C12A7 mainly arises from the structural disorder at lower temperature, while the thermal fluctuation dominates at temperatures higher than ~ 400 K.

The characteristic phonon energy, 32 meV or 260 cm^{-1} in wave number, is presumably related to Raman bands observed in the low-energy region ($<400\text{ cm}^{-1}$). Figure 10 shows the calculated density of states for Raman-active modes. It is found that the vibrations at frequencies below 400 cm^{-1} are exclusively ascribed to Ca^{2+} -related modes. It has been demonstrated that an electron promoted to the conduction band of C12A7 forms

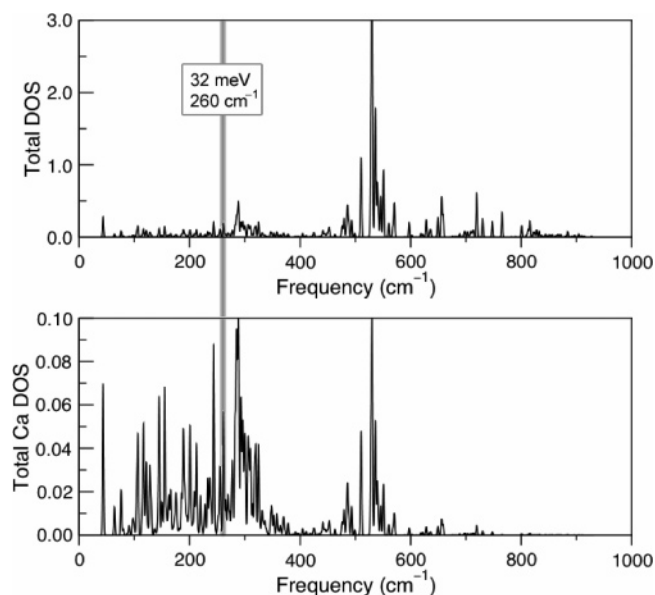


Figure 10. Calculated density of states (DOS) for Raman-active modes of the lattice framework: (a) total DOS and (b) total Ca contribution. Note the difference in vertical scales.

a polaron, which is associated with considerable displacements of Ca^{2+} ions.¹⁹ The magnitude of the Ca^{2+} ions displacements correlates well with the splitting of the polaron level from the conduction band. Thus, since the polaron and immobile hole in the valence band form the exciton, we suggest that the phonon responsible for the Urbach tail is the vibration modes associated with Ca^{2+} ions.

On the other hand, the origin of the structural disorder is attributable to the random distribution of the extraframework anions. The anion incorporation in a cage causes the displacement of two Ca^{2+} ions on the S_4 axis toward the cage center, shortening their distance, d_{S4} , typically by $\sim 10\%$ for singly charged anions.¹⁹ In sample 7, $1/3$ of the cages are occupied by F^- ions, while the others are empty. Because of the random distribution of the F^- ions over the cages, the distorted cages are distributed randomly, resulting in the structural disorder. Thus, the fluctuation of the Ca^{2+} ion is induced by both the thermal vibrations and the structural disorder; the anion incorporation contributes to the Urbach tail in the F^- ion encaged C12A7. We note that the contribution due to the structural disorder is expected to be larger in the case of the doubly charged extraframework anions such as O^{2-} and O_2^{2-} , since they induce larger shortening in d_{S4} with approximately $\sim 20\%$.²¹ Moreover, an extraframework O^{2-} anion occupies an off-center configuration and forms a dative bond with the Al^{3+} ion in the cage wall, which, in turn, displaces toward the cage center. Thus, the local distortion of the lattice framework is much stronger in this case.

Nevertheless, the structural disorder, defined by term X , in C12A7 is not so strong as compared to a conventional rigid crystal, where structural disorder is caused by anion vacancy formation. For example, the value of X determined for a doped BaCeO_3 ,³³ where substitution of aliovalent cation forms oxide ion vacancies, is 6.2, which is about three times larger than that in C12A7 even though the concentration of vacancies was ~ 3 times less than that of the extraframework anions in C12A7.

6. Conclusions

C12A7 has an unusual crystal lattice, which can be used to incorporate large concentrations of various negatively charged

species and study their properties. We have shown that by choosing an appropriate treatment of as grown C12A7 one can control the chemical composition of the extraframework. In particular, nearly complete substitution of all extraframework species by F^- or OH^- ions can be realized.

Optical measurements for C12A7 with several kinds of encaged anions (O^{2-} , O^- , O_2^- , O_2^{2-} , OH^- , and F^-), together with theoretical calculations of their electronic structure and optical excitations, make it possible to assign the absorption edges and bands in the UV–vis region. Extraframework anions of OH^- , O^{2-} , and active oxygen anions (O^- , O_2^{2-} , and O_2^-) give rise to absorption edges or bands below the fundamental edge, which is due to the transition from the top of the valence band to the bottom of the framework conduction band. The absorption edge shifts to the lower energy side upon the incorporation of the anions in the order $\text{F}^- > \text{OH}^- > \text{O}^{2-} > \text{oxygen radicals}$. Thus, the absorption edge is controlled by the chemical identity and relative concentrations of the extraframework species and can be varied from ~ 4 to ~ 6 eV.

The edges for OH^- and O^{2-} ions are assigned as transitions from localized anion states to FCB, while those for oxygen radicals are likely from the VB to the anion state. Elimination of the oxygen-related extraframework anions by F^- ion substitution allows us to observe the fundamental absorption edge originated from the lattice framework. A good correlation between our results and the reported excitation energies, for example, for O_2^- and O_2^{2-} ions in other host lattices, further supports our view that C12A7 can be used as a matrix for characterization of anions that cannot be generated in other materials at sufficiently large concentrations.

In addition, the analysis of the Urbach tail structure makes it possible to estimate the intrinsic exciton formation energy as 6.6 eV, which is smaller than the intrinsic band gap energy (difference between the VB and FCB edges) by the exciton binding energy. The thermal vibration and the structural disorder, both of which are likely associated with the displacement of Ca^{2+} ions, contribute to the Urbach energy. In particular, the structural contribution is due to an inhomogeneous displacement of Ca^{2+} ions caused by a random distribution of anions (F^- ions) over the cages.

Acknowledgment. This work is supported by the Grant-in-Aid for Creative Scientific Research (No. 16GS0205) from Japanese Society for the Promotion of Science, and in part by the Grant-in-Aid for Young Scientists B (No. 17750193) from the Japanese Ministry of Education, Culture, Sports, Science and Technology. The calculations were carried out on the UCL Central Computing Cluster C3. We also thank K. Kawamura for experimental assistance and J. L. Gavartin and K. McKenna for their comments on the manuscript.

Supporting Information Available: F^- exclusion process and complete ref 28. This material is available free of charge via the Internet at <http://pubs.acs.org>.

References and Notes

- (1) *Calcium Aluminate Cements 2001*; Mangabhai, R. J., Glasser, F. P., Eds.; The University Press: Cambridge, UK, 2001.
- (2) Hafner, H. C.; Kreidel, N. J.; Weidel, R. A. *J. Am. Ceram. Soc.* **1958**, *41*, 315–323. Wallenberger, F. T.; Weston, N. E.; Dunn, S. A. *J. Non-Cryst. Solids* **1990**, *124*, 116–119. Shirnov, G. S.; Chatterjee, A. K.; Zhmoldin, G. L. *J. Mater. Sci.* **1973**, *8*, 1278–1282. Kim, S.-W.; Miyakawa, M.; Hayashi, K.; Sakai, T.; Hirano, M.; Hosono, H. *J. Am. Chem. Soc.* **2005**, *127*, 1370–1371.
- (3) Nurse, R. W.; Welch, J. H.; Majumdar, A. J. *Trans. Br. Ceram. Soc.* **1965**, *64*, 323–332. Imlach, J. A.; Glasser, L. S. D.; Glasser, F. P. *Cem. Concr. Res.* **1971**, *1*, 57–61. Zhmoldin, G. I.; Chatterjee, A. K. *Cem. Concr. Res.* **1984**, *14*, 386–396. Edmonds, R. N.; Majumdar, A. J. *Cem. Concr. Res.* **1988**, *18*, 473–478.
- (4) Hayashi, K.; Hirano, M.; Hosono, H. *J. Phys. Chem. B* **2005**, *109*, 11900–11906.
- (5) Jeevaratnam, J.; Glasser, F. P.; Glasser, L. S. D. *J. Am. Ceram. Soc.* **1964**, *47*, 105–106.
- (6) Williams, P. P. *Acta Crystallogr.* **1973**, *B29*, 1550–1551.
- (7) Feng, Q.-L.; Glasser, F. P.; Alan-Howie, R.; Lachowski, E. E. *Acta Crystallogr.* **1988**, *C44*, 589–592. Fujita, S.; Suzuki, K.; Ohkawa, M.; Mori, T.; Iida, Y.; Miwa, Y.; Masuda, H.; Shimada, S. *Chem. Mater.* **2003**, *15*, 255–263.
- (8) Hosono, H.; Abe, Y. *Inorg. Chem.* **1987**, *26*, 1192–1195. Stösser, R.; Nofz, M.; Gessner, W.; Schröter, C.; Kranz, G. *J. Solid State Chem.* **1989**, *81*, 152–164.
- (9) Hayashi, K.; Hirano, M.; Matsuishi, S.; Hosono, H. *J. Am. Chem. Soc.* **2002**, *124*, 738–739. Hayashi, K.; Li, Q.; Nishioka, M.; Matsuishi, S.; Torimoto, Y.; Hirano, M.; Sadakata, M.; Hosono, H. *Electrochem. Solid-State Lett.* **2002**, *5*, J13–J16. Hayashi, K.; Matsuishi, S.; Ueda, N.; Hirano, M.; Hosono, H. *Chem. Mater.* **2003**, *15*, 1851–1854.
- (10) Hayashi, K.; Matsuishi, S.; Hirano, M.; Hosono, H. *J. Phys. Chem. Soc. B* **2004**, *108*, 8920–8925. Hayashi, K.; Ueda, N.; Hirano, M.; Hosono, H. *Solid State Ionics* **2004**, *173*, 89–94.
- (11) Yang, S.; Kondo, J. N.; Hayashi, K.; Hirano, M.; Domen, K.; Hosono, H. *Chem. Mater.* **2004**, *16*, 104–110.
- (12) Hayashi, K.; Hirano, M.; Hosono, H. *Chem. Lett.* **2005**, *34*, 586–587.
- (13) Hayashi, K.; Matsuishi, S.; Kamiya, T.; Hirano, M.; Hosono, H. *Nature* **2002**, *419*, 462–465. Hayashi, K.; Toda, Y.; Kamiya, T.; Hirano, M.; Yamanaka, M.; Tanaka, I.; Yamamoto, T.; Hosono, H. *Appl. Phys. Lett.* **2005**, *86*, 22109–1–3. Matsuishi, S.; Hayashi, K.; Hirano, M.; Hosono, H. *J. Am. Chem. Soc.* **2005**, *127*, 12454–12455. Hayashi, K.; Sushko, P. V.; Shluger, A. L.; Hirano, M.; Hosono, H. *J. Phys. Chem. B* **2005**, *109*, 23836–23842.
- (14) Miyakawa, M.; Kamioka, H.; Hirano, M.; Kamiya, T.; Sushko, P. V.; Shluger, A. L.; Matsunami, N.; Hosono, H. *Phys. Rev. B* **2006**, *73*, 205108–1–7.
- (15) Matsuishi, S.; Toda, Y.; Miyakawa, M.; Hayashi, K.; Kamiya, T.; Hirano, M.; Tanaka, I.; Hosono, H. *Science* **2003**, *301*, 626–629.
- (16) Lacerda, M.; Irvine, J. T. S.; Glasser, F. P.; West, A. R. *Nature* **1988**, *332*, 525–526. Irvine, J. T. S.; West, A. R. *Solid State Ionics* **1990**, *40/41*, 896–899. Sushko, P. V.; Shluger, A. L.; Hayashi, K.; Hirano, M.; Hosono, H. *Phys. Rev. B* **2006**, *73*, 14101–1–10.
- (17) Nandi, A. K.; Chaudhari, A. K.; Thiagarajan, S.; Ghosh, S. B. *Ceram. Trans.* **1993**, *92*, 81–82. Hayashi, K.; Hirano, M.; Hosono, H. *J. Mater. Res.* **2002**, *17*, 1244–1247.
- (18) Bartl, H.; Scheller, T. N. *Jb. Miner. Mh.* **1970**, *35*, 547–552.
- (19) Sushko, P. V.; Shluger, A. L.; Hayashi, K.; Hirano, M.; Hosono, H. *Phys. Rev. Lett.* **2003**, *91*, 126401–1–4. Sushko, P. V.; Shluger, A. L.; Hayashi, K.; Hirano, M.; Hosono, H. *Thin Solid Films* **2003**, *445*, 161–167. Sushko, P. V.; Shluger, A. L.; Hayashi, K.; Hirano, M.; Hosono, H. *Mater. Sci. Eng. C* **2005**, *25*, 722–726.
- (20) Sushko, P. V.; Shluger, A. L.; Hayashi, K.; Hirano, M.; Hosono, H. *Appl. Phys. Lett.* **2005**, *86*, 92101–1–3.
- (21) Sushko, P. V.; Shluger, A. L.; Hayashi, K.; Hirano, M.; Hosono, H. *Phys. Rev. B* **2006**, *73*, 045120–1–13.
- (22) Watauchi, S.; Tanaka, I.; Hayashi, K.; Hirano, M.; Hosono, H. *J. Cryst. Growth* **2002**, *237–239*, 496–502.
- (23) Park, J.-K.; Shimomura, T.; Yamanaka, M.; Watauchi, S.; Kishio, K.; Tanaka, I. *Cryst. Res. Technol.* **2005**, *40*, 329–333.
- (24) Kamiya, T.; Hosono, H. *Jpn. J. Appl. Phys.* **2005**, *44*, 774–782.
- (25) A sample experiencing many annealing steps tends to form pores inside, which cause a tail in the higher energy range of the spectrum due to the Mie scattering.
- (26) Zacate, M. O.; Grimes, R. W. *J. Phys. Chem. Solids* **2002**, *63*, 675–683.
- (27) Sushko, P. V.; Shluger, A. L.; Catlow, C. R. A. *Surf. Sci.* **2000**, *450*, 153–170. Sulimov, V. B.; Sushko, P. V.; Edwards, A. H.; Shluger, A. L.; Stoneham, A. M. *Phys. Rev. B* **2002**, *66*, 024108–1–14.
- (28) Frisch, M. J. et al. *GAUSSIAN 98*, Revision A.7; Gaussian Inc.: Pittsburgh, PA, 1998.
- (29) Che, M.; Tench, A. J. *Adv. Catal.* **1983**, *32*, 1–148.
- (30) McMillan, P.; Piriou, B. *J. Non-Cryst. Solids* **1983**, *55*, 221–242.
- (31) Sumi, H.; Toyozawa, Y. *J. Phys. Soc. Jpn.* **1971**, *31*, 342–358. Godmanis, I. T.; Trukhin, A. N.; Hübner, K. *Phys. Status Solidi B* **1983**, *116*, 279–287.
- (32) Cody, G. D.; Tiedje, T.; Abeles, B.; Brooks, B.; Goldstein, Y. *Phys. Rev. Lett.* **1981**, *47*, 1480–1483.
- (33) He, T.; Ehrhart, P.; Meuffels, P. J. *Appl. Phys.* **1996**, *79*, 3219–3223.
- (34) Saito, K.; Ikushima, J. *Phys. Rev. B* **2000**, *62*, 8584–8587. Skuja, L.; Kajihara, K.; Ikuta, Y.; Hirano, M.; Hosono, H. *J. Non-Cryst. Solid* **2004**, *345/346*, 328–331.

- (35) Rolfe, J.; Lipsett, F. R.; King, W. J. *Phys. Rev.* **1961**, 123, 447–454.
- (36) Fischer, F.; Gründig, H.; Hilsch, R. *Z. Phys.* **1966**, 189, 79–96.
- (37) Andersen, T.; Baptista, J. L. *Phys. Status Solidi B* **1971**, 44, 29–38.
- (38) Bryukvin, V. V.; Penzina, E. E. *Opt. Spectrosc.* **1992**, 73, 66–69.
- (39) Kurobori, T.; Taniguchi, S.; Takeuchi, N. *J. Mater. Sci.* **1992**, 27, 6352–6356.
- (40) Pacchioni, G.; Ierano, G. *Phys. Rev. B* **1998**, 57, 818–832.
- (41) Andrews, L. *J. Mol. Spectrosc.* **1976**, 61, 337–345.